

Micro-Capillary Electrochemical and Microscopic Investigations of Massive and Individual Micrometer-Sized Powder Particles of Stainless Steel 316L

Y. Hedberg^{1,2,*}, S. Virtanen², I. Odnevall Wallinder¹

¹ KTH Royal Institute of Technology, Div. Surface and Corrosion Science, Dept. Chemistry, Drottning Kristinas väg 51, SE-10044 Stockholm, Sweden

² Department of Materials Science (LKO), University of Erlangen-Nuremberg, Martensstrasse 7, D-91058 Erlangen, Germany

*E-mail: yolanda@kth.se

Received: 22 September 2012 / Accepted: 31 October 2012 / Published: 1 December 2012

Material properties, corrosion, and metal release from stainless steel powders are important factors to assess any occupational health hazards. This paper elucidates the corrosion behavior of stainless steel particles (inert-gas-atomized AISI 316L powders sized < 45µm, polished and non-polished) compared with corresponding massive low-sulfur bulk sheet material. Electrochemical measurements using a microcapillary technique are compared with ex-situ optical and scanning electron microscopy imaging and electron dispersive X-ray spectroscopy elemental analysis on the same area of individual particles. Non-polished 316L particles were significantly more passive compared to polished massive sheet and polished particles that in general showed a similar corrosion behavior. Corrosion was not induced by bulk compositional differences but could be attributed to surface inhomogeneities. The results are in agreement with the high passivity of non-polished particles in macroscopic studies, an effect caused by a unique surface oxide, characterized in part I of this paper series.

Keywords: stainless steel, surface oxide, powder, pitting corrosion, passive films

1. INTRODUCTION

The austenitic stainless steel grade AISI 316, containing 16.5-18.5 wt% Cr, 10.5-13 wt% Ni, and 2.5-3 wt% Mo, is widely used in settings with high requirement on pitting corrosion resistance such as marine environments [1]. For biomedical applications, grade 316L is more commonly used [2] due to its low carbon content (≤ 0.03 wt %), its resistance to sensitization [1], and its improved corrosion resistance compared with 316 as long as the sulfur content is kept at low levels (≤ 0.001

wt%). The presence of MnS-inclusions or other inclusions or impurities are uncommon in low-sulfur 316L grades [3]. Differently orientated grains [3] or oxide grain boundaries [4] have, in the absence of inclusions, been reported as pit initiation sites for low-sulfur 316L when exposed to chloride-containing environments. Pit initiation and the possibility of repassivation depend on material and prevailing environmental conditions [5]. These processes are largely determined by the formation of a salt layer [6-7], on the chloride content in solution [8] and on the driving force for chlorides to electromigrate to the site of the pit (i.e., the pit pH [9-10], the charge of released ions inside the pit [10], and the surface charge of the pit area [11]). Finally, the growth of the pit, which is autocatalytic [5], may be controlled by diffusion in the case of a salt layer [10] and then grow hemispherically [5]. In the absence of a salt layer, pit growth has been reported to be independent of mass transport [7].

Grade 316L contains Cr and Mo, elements of high importance upon pit initiation and pit repassivation [6, 12-14]. It has been suggested that both Cr and Mo are important for the resistance of the passive film against pit nucleation and moreover that pit growth and repassivation are rather determined by the bulk alloy components than of elements in the passive film [12]. The degree of crystallinity of the passive film depends on the Cr bulk content [15-16] in addition to passivation time [17]. A high Cr bulk content (> 16 wt%) has been reported to correlate with higher disordered passive films [15-16] and hence a lower probability for oxide grain boundaries.

Material properties, corrosion, and the release of metals from stainless steel in biological fluids are important factors for any induced toxicity and have, with this end-point in mind, been investigated in a large research effort screening different massive stainless steel grades [18]. Since grade 316L released the highest amount of nickel, it was selected for further in-depth studies. For micrometer-sized stainless steel powders, potential occupational health hazards are predominantly induced via inhalation (depending on particle size) or dermal contact. The metal release process was therefore investigated for differently sized gas-atomized 316L powders in different synthetic fluids of relevance for inhalation [19-21] and dermal contact [22]. Moreover, surface changes during exposure [20], and the influence of the crystallographic structure and particle size on the metal release process have been investigated [20, 23-24]. Inert-gas-atomized powder particles sized less than 45 μm were shown to possess a comparable microstructure (austenite) and composition as massive 316L [23]. The extent of released metal from the gas-atomized 316L powder (<45 μm) was lower compared with as-received massive 316L sheet when exposed both in artificial lysosomal fluid (pH 4.5) and Gamble's solution (pH 7.4) [24]. In order to identify how the 316L particles behave from a corrosion perspective in comparison to massive 316L, several studies were initiated. Macroscopic electrochemical studies suggested a higher corrosion resistance of the gas-atomized 316L powder (<45 μm) compared with abraded massive sheet [25]. No conclusive comparison was possible in that study since non-abraded particles were compared with abraded massive sheet and an accurate estimation of the active surface area of immobilized particles on the electrode surface was difficult to assess.

This study therefore aims to clarify these issues further and compare the corrosion behavior of grade 316L as massive sheet and as a powder by investigating polished and non-polished powder particles compared to abraded massive sheet of the same surface area (micrometer-scale) at similar exposure conditions. In-depth characterization of the surface oxide and passive properties of individual

particles using different electrochemical, spectroscopic, and microscopic techniques are published in parallel in this journal [26].

2. MATERIALS AND METHODS

2.1. Materials and preparation

The bulk alloy composition of the investigated massive sheet (supplied by Thyssen Krupp, Germany) and the gas-atomized powder (supplied by Arcam, Sweden, produced by Anval AB, Sweden) is given in Table 1.

According to supplier information, 87% of the particles were sized $<44\ \mu\text{m}$, 32% $<22\ \mu\text{m}$ (32%), and 0.7% $<5.5\ \mu\text{m}$. Previously reported particle size distribution measurements in solution (phosphate buffered saline, pH 7.4) revealed a median diameter of $22.5\ \mu\text{m}$ (by volume) and $11.3\ \mu\text{m}$ (by number) [19]. Detailed information on morphology [19], size distribution [19, 22], and microstructure [23] is given elsewhere. Detailed surface characterization is given in the parallel paper (part I) published in this issue [26].

Table 1. Nominal bulk composition of the 316L powder sized $<45\ \mu\text{m}$ and the massive sheet based on supplier information.

	Fe (wt %)	Cr (wt %)	Ni (wt %)	Mo (wt %)	Mn (wt %)	Si (wt %)	C (wt %)
$< 45\ \mu\text{m}$	68.9	16.8	10.3	2.1	1.4	0.5	0.03
Massive sheet	68.7	16.6	10.6	2.1	1.0	0.4	0.03
	S (wt %)	P (wt %)	Ti (wt %)	Nb (wt %)	Co (wt %)	Cu (wt %)	
$< 45\ \mu\text{m}$	0.01	0.03	-	-	-	-	
Massive sheet	0.001	0.02	0.03	0.01	0.2	0.3	

2.2. Micro-electrochemistry of massive 316L

The microcell consisted of a glass capillary with a diameter of $159\ \mu\text{m}$ filled with the electrolyte and containing the auxiliary electrode (platinum wire), while the reference electrode (Ag/AgCl (3 M KCl)) was connected via an electrolytic bridge. The glass capillary was drawn, the tip was polished, and a silicone rubber O-ring was used to seal between the capillary and the sample surface. Typical images of such glass capillaries are given in [27]. A high resolution potentiostat (Jaissle IMP 83 PC T-BC) with a detection limit of the current of $10\ \text{fA}$ was used with a sampling rate of $9\ \text{Hz}$. The capillary was placed in an objective holder to enable the microscopic investigation (Leica

DM LS2, lateral resolution of about 1 μm) of the same area. Detailed information on the micro-electrochemical setup is given elsewhere [12, 27-29].

Anodic polarization curves were generated for both massive sheet and powder particles of 316L (c.f. next section for particle set-up). Samples were polished to 1 μm with diamond paste one day prior to the measurement, cleaned ultrasonically in ethanol for 5 min, dried in air using a fan and stored in air at ambient conditions. This pre-treatment and ageing were conducted for all experiments to allow an equal growth of the surface oxide. The start potential was set to -500 mV (Ag/AgCl) in the case of massive sheet and non-polished particles, and -300 mV for the polished particles. The end potential was in all cases 1200 mV. Before starting the potential scan, the system was allowed to equilibrate for some minutes. The scan rate was set to 1 mV/s. Two different electrolytes were used, 1 M NaCl and 0.1 M HCl.

For mass transfer calculations, the current-potential curves were transferred into current-time curves. The area was estimated using the Origin software, with the passive current as (prolonged) the linear baseline.

2.3. Micro-electrochemical set-up for powder particles

The experiments were carried out for both polished and non-polished particles. In order to allow polishing of the particle surface, the particles were embedded in a graphite filled conductive polymer resin (Technotherm 3000, Heraeus Kulzer, Germany) suitable for scanning electron microscopy measurements. Cylindrical samples ($\text{\O} 30 \text{ mm}$) were generated via a hot-mounting process operating at 180°C and 70 bar for 12 min. The sample was ground and subsequently polished down to 1 μm . The polishing success was confirmed by means of light microscopy imaging (Nikon eclipse LV150). Since it was difficult to identify the capillary position on the black resin, its position was first identified and adjusted on a polished massive sheet. Several images were generated on the approximate capillary position on the resin and saved prior to analysis after which the capillary was positioned on the desired area. Measurements were initiated when no capillary leakage was occurring and electrical contact between the sample and the capillary was confirmed. After the measurement, the exact corroded area position was identified and several images were collected and compared with images generated prior to exposure. This approach did unfortunately not allow identification of the exact area of corrosion during or directly after the measurement. Compared to the measurements of massive 316L, a lower percentage of measurements were successful (5 measurements) on the polished particles due to larger leakage problems (higher surface roughness compared with massive 316L) and/or difficulties to identify the exact capillary position (black background).

An experimental set-up that allowed fixation of the particles on a conductive but non-reactive surface was developed to enable measurements on non-polished particles. Since the non-polished particles ($\text{\O} < 45 \text{ }\mu\text{m}$) in this context represent a rough surface, the probability for leakage from the microcapillary was increased. Carbon tape and silver tape were both found to be too reactive for these measurements. A paraffin impregnated graphite electrode (PIGE) was identified as the most suitable set-up since the particles could easily become immobilized and fixed on the surface (by heating the

PIGE prior to pressing it into the powder) [30-32]. The PIGE showed in addition negligible background currents in both electrolytes investigated. It was necessary to allow the heated PIGE to cool down some seconds prior to particle fixation in order to avoid a complete surface coverage by the paraffin.

For all particle measurements, the 0.1 M HCl electrolyte was aggressive enough to distinguish corrosion reactions taking place on the particles from the background current of the embedding or substrate material.

2.4. Microscopic investigations

Apart of optical microscopy investigations (Leica DM LS2), field emission scanning electron microscopy imaging (FESEM, S-4800, Hitachi) were conducted to assess changes in surface morphology and corrosion product formation upon exposure. Elemental analysis was performed by means of energy dispersive x-ray spectroscopy, EDS (EDS, EDAX Genesis).

3. RESULTS AND DISCUSSION

3.1. Pitting corrosion of massive 316L

The micro-electrochemical set-up, equipped with an optical microscope, was employed to study the occurrence of pitting corrosion at different surface locations of massive 316L. A range of unique measurements on dissimilar areas was performed to achieve a statistically relevant surface distribution (9 and 8 measurements in 1 M NaCl and 0.1 M HCl, respectively). A compilation of pitting potentials (Fig. 1), when observed, corresponding current-potential curves (Fig. 2), and corresponding areas (Fig. 3) identified after the measurements on massive sheet are presented in Figs. 1-3. A large variety of pitting potentials (between 540 and 1050 mV (Ag/AgCl) in 1M NaCl) was evident at different locations of the sample, Fig. 1. These observations are typical for micro-electrochemical measurements using very small capillary diameters (here \varnothing 159 μm) on stainless steel exposed in chloride solutions. Previous findings for AISI 304 stainless steel in 1 M NaCl revealed comparable (between 500 and 1100 mV (SCE)) pitting potentials when using a capillary diameter of 150 μm [29]. In that study [29], a clear correlation between increasing variation in pitting potentials (and higher average pitting potential) with decreasing capillary diameters was shown, where capillary diameters larger than 450 μm showed comparable pitting potential values for macroscopic measurements. The deviation between different measurements of the pitting potential increased strongly with decreasing capillary diameter, for diameters less than 450 μm [29, 33]. This was explained by a lower probability of the presence of pitting susceptible sites (defect, inclusion, etc.) at smaller areas [29, 33]. It is notable that previous findings on macroscopic pitting corrosion measurements of vacuum melted AISI 316L (very low sulfur and other impurities) in 1 M NaCl

revealed an average pitting potential of about 300 mV (SCE) [3], findings in agreement with mm-sized capillary measurements on grade 304 in the same electrolyte [about 300-400 mV (SCE)] [29].

The massive 316L sheet of this study is a high-purity grade containing only 0.001 wt% S and 0.03 wt% C. This was clearly reflected in the measurements, as no correlation between pitting corrosion and areas with more visible “inclusions” (observed as small ($< 10 \mu\text{m}$) black surface features, e.g., Fig. 3b) were found. The microstructure was quite frequently visible (seen as the dendritic structure) after measurements in both solutions, similar to observations from etching, Fig. 3e. These findings could indicate a grain orientation dependent initiation of pitting corrosion, as suggested in [3], rather than MnS-initiated pitting corrosion, as previously suggested as main initiation sites for other stainless steel grades, in particular for higher sulfur grades [29, 33-37]. The results are consistent with literature findings, which show the lack of stable pit growth for grades of very low sulfur content (0.001 wt %) and/or MnS inclusions sized less than $1 \mu\text{m}$ [29, 33]. Both grain sizes and orientation for the investigated massive 316L sheet have previously been reported [23]. These findings reveal a typical grain size of approximately 2-10 μm in diameter. This suggests that a wide range of grain orientations and boundaries should be present within the capillary area. Another possible explanation for the surface heterogeneity could be local surface oxide defects, in particular present at grain boundaries [4]. It was however not possible to exclude any of these effects and any possible explanations are only speculative.

Slightly lower pitting potentials were observed in the more acidic 0.1 M HCl solution (287-930 mV) compared with 1 M NaCl (540-1050 mV), Fig. 1. However, cases of no pitting corrosion were in addition observed in both solutions (2 cases out of 8 in 1 M NaCl, and 3 cases out of 9 in 0.1 M HCl), Fig. 1.

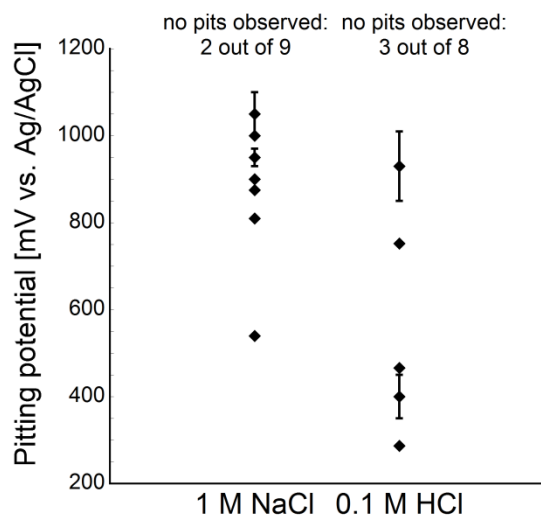


Figure 1. Pitting potentials measured on massive 316L in 9 independent measurements (1 M NaCl, left) and 8 independent measurements (0.1 M HCl, right) using a micro-capillary technique. Error bars are presented for the cases with broad, rather than sharp, pitting breakdown.

Obtained images after the measurements revealed in these cases (Figs. 3a and b) no visible surface change (the black spots on the image of the 1 M NaCl solution are salt crystals (visible first after drying of droplet), Fig. 3a), only the imprint of the silicon rubber of the capillary was observed. Corresponding current-potential curves showed a long passive range and the typical oxidation peak at approximately 1000 mV (Ag/AgCl), immediately prior to the oxygen evolution region. This preceding peak could be related to the thickening of the inner Fe(III) and Cr(III) oxide layer, as previously discussed in [38]. In the transpassive region, chromium(III) is oxidized to chromium(VI) [8]. The current-potential curves of samples exposed in 0.1 M HCl showed more metastable pitting, observed as current transients and/or step-wise breakdown events, as compared with the 1 M NaCl solution with a passive range without metastable pitting and, if any, a clear one-step breakdown, Fig. 2. The corrosion potential was significantly lower in 1 M NaCl (between -415 and -450 mV) compared with 0.1 M HCl (between -267 and -349 mV). In macroscopic measurements, the current-potential curves and pitting potentials of the two different electrolytes are expected to differ to an even larger extent [8].

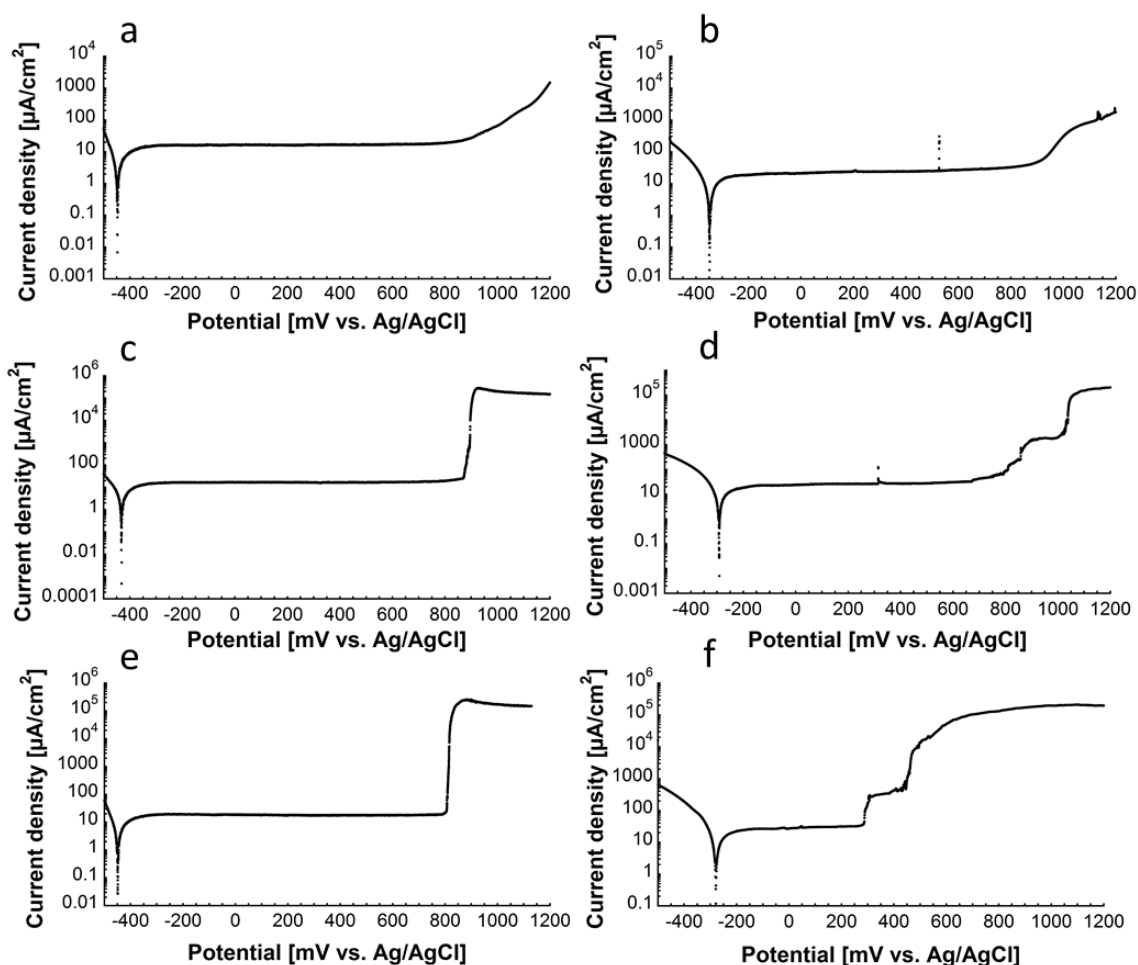


Figure 2. Current density – potential curves corresponding to selected micro-capillary measurements of massive sheet of 316L presented in Fig. 1. a, c, e: 1 M NaCl; b, d, f: 0.1 M HCl.

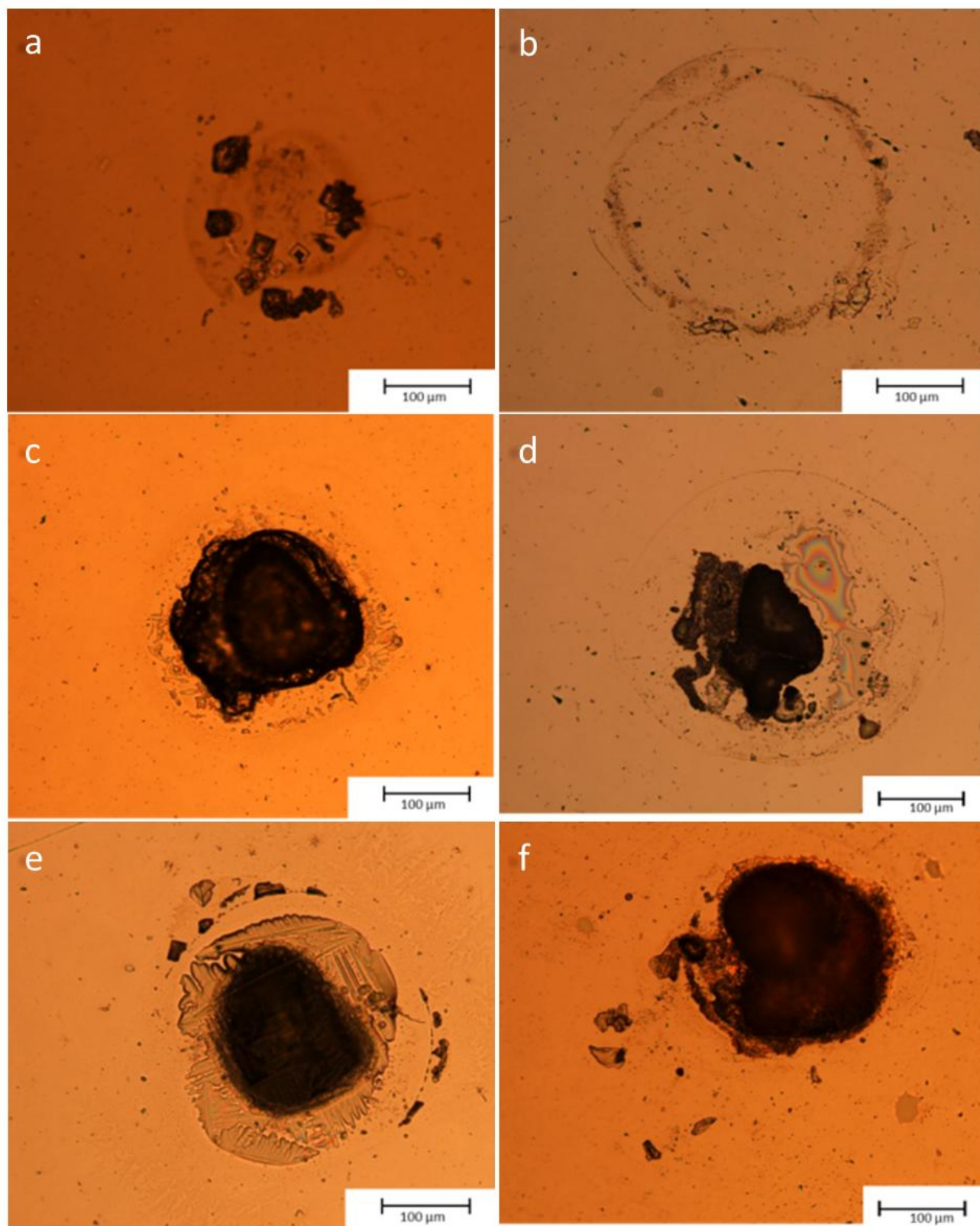


Figure 3. Optical microscopy images of areas after micro-capillary electrochemical measurements on massive 316L. Each image correlates to the electrochemical measurements presented in Fig. 2 (Fig. 3a corresponds to Fig. 2a, etc.).

3.2. Corrosion of polished particles of the 316L powder

Electrochemical studies of inert-gas-atomized 316L polished particles ($< 45\mu\text{m}$) were conducted using a similar approach as for massive sheet [12, 27-29]. All measurements were performed in the most aggressive solution, 0.1 M HCl, to enable distinction between the current related to particle corrosion and the background current. Typical overview images and images of higher magnification, assembled after exposure and during post-evaluation, are presented in Figure 4. The corroded area was easily identified by comparing areas prior to and after exposure, and by identifying changes in terms of dissolved particles, changes in particle appearance (from white to brown) and/or partly dissolved, shrunk particles. The relative extent of corrosion for each particle within the capillary area was compared with obtained current-potential curves. Presented absolute values of the current density need to be considered with caution since an accurate surface area of the particles is difficult to assess. The actual surface area was estimated (based on a visual estimation of the particle surface distribution within the capillary area) to be 2-5 times lower than used in the calculation of the current density (using an area calculated from the capillary diameter). This means that the current density should be approximately 2-5 times higher than presented. This effect is important to consider when comparing different measurements (section 3.4.).

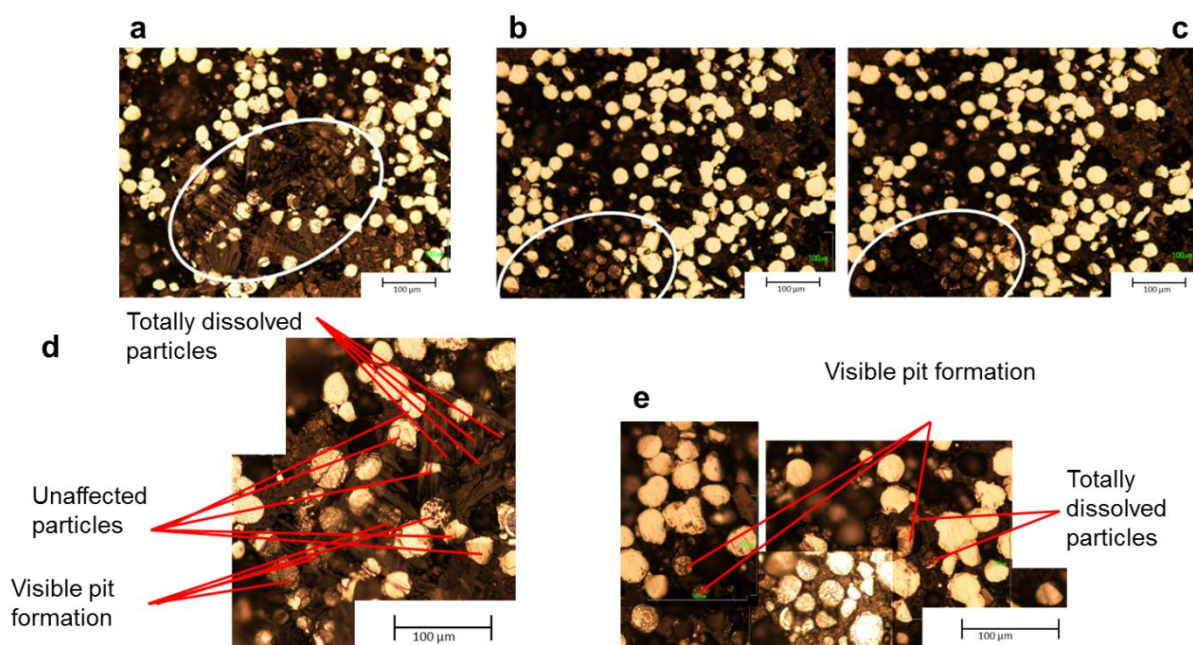


Figure 4. Two examples (1: a and d; 2: b, c, and e) of optical microscopy images of capillary areas of embedded polished 316L particles before (b) and after micro-electrochemical measurements (a, c, d-e (magnified areas)).

Based on Faraday's law [39] and the assumptions that oxygen evolution is negligible and that metals are released in proportion to the bulk composition, i.e. 72% Fe (oxidation state 2), 18% Cr

(oxidation state 3) and 10 % Ni (oxidation state 2), the transferred mass can be calculated according to eq. (1):

$$m = \frac{I \times t}{F} \times \frac{0.72M_{Fe} + 0.18M_{Cr} + 0.10M_{Ni}}{0.72z_{Fe} + 0.18z_{Cr} + 0.10z_{Ni}} \quad (1)$$

where m is the transferred mass [g], I is the current [A], t is the time [s], F is the Faraday constant [96 487 C/mol], M is the molar mass [g/mol], and z is the number of transferred electrons, e.g. assumed to be 2 in the case of iron. Another necessary assumption was that the particles were ideally spherical and of identical size. Based on these assumptions, this calculation suggests that the measured charge in different measurements would correspond to the dissolution of 20-84 complete particles with a diameter of 20 μm , or 2.5-10.4 particles sized 40 μm in diameter (twice as many for hemispheres). For example, for the measurements shown in Figs. 4a and c, the transferred mass charge would correspond to the dissolution of 35 complete particles with a diameter of 20 μm , or 4 particles with a diameter of 40 μm . Even though this semi-quantitative estimation is based on many assumptions, it indicates a reasonable approximation of the dissolved particle mass, in concordance with visual observations.

All measurements revealed a highly heterogeneous corrosion process with completely unaffected particles, visible strong pitting within single particles, and completely dissolved particles. Corrosion occurred independently of the position within the area in contact with the capillary (i.e., neither close to the sealing interface nor in the middle of the capillary), and of the extent of corrosion of adjacent particles. One of the corroded areas (Fig. 5) was investigated in more detail by means of SEM/EDS after the micro-capillary measurements aiming to address underlying reasons behind this heterogeneous corrosion attack. The corresponding current-potential curve showed for this area an early breakdown directly after the corrosion potential and a high current throughout the entire potential range. However, since the post-evaluated optical image (Fig. 5) showed the whole range of corrosion attacks, from no effect to complete dissolution of different particles, also visualized by means of SEM, this suggests that the current-potential curve is not able to predict the corrosion distribution of complex systems with several particles. No direct correlation was observed between different locations of the particles (within the capillary area or in relation to their distance to other corroded particles) and the extent of corrosion. Compositional analysis of particles of varying degree of corrosion (Fig. 5) showed no significant differences, Table 2. EDS mapping on randomly corroded particles showed a homogenous composition within single particles (data not shown). Differences in particle composition could hence not explain the observed corrosion behavior.

SEM images of the capillary area shown in Fig. 5 are presented in Fig. 6. Fig. 6a shows a nearly non-corroded particle, positioned in the close vicinity to several corroded particles. This image combined with Fig. 6b, displaying several pits initiated close to the particle/resin interface. This suggests that the presence of crevices may be a reason for pit initiation, as well as the very close vicinity to other corroded particles (as in this case). However, numerous other pits were seemingly randomly initiated (Figs. 6b (particle in the middle) and 6d), and several pits were often observed

within a single particle (Fig. 6). This suggests that pit propagation is sufficiently slow compared with new pit initiation and/or that several pits were repassivated. On severely corroded particles (Fig. 6c), on the other hand, a large volume of the particles was dissolved, while the remaining surface still was intact to a large extent. These observations are in concordance with findings for massive stainless steel, where pit growth was favored compared with initiation of new other pits, showing e.g. only one deep pit and at the same time nearly unaffected surfaces within the same capillary area (e.g. Fig. 3d). This suggests that pit growth was more favorable compared with new pit initiation. This is probably related to the relatively passive surface oxide [1] and that any observed pits on these areas are metastable or repassivated. Despite the relatively larger sulfur content of the 316L powder compared with massive 316L (0.01 vs. 0.001 wt %), typically connected with MnS inclusions [29, 33], no evidence for micron-sized MnS inclusions was found. The reason could be related to the manufacturing process of gas-atomized particles with approximately 13 wt% of Mn (relative metal fraction) in the surface oxide [20] and the enrichment of S, both within oxide nanoparticles at the surface and in the surface oxide, as presented and discussed in detail in [40].

Figure 6e displays a magnified area of the corroded area within a stable pit. Its morphology does not seem to directly reflect the microstructure (i.e. the dendritic microstructure for these particles as presented in [23]), but rather a pore-like morphology. A similar pit corrosion morphology has been observed for massive 316L exposed in 0.5M H₂SO₄ [41]. The formation of ordered nano-pores has also been observed for electropolished stainless steel grade 316L exposed in perchloric acid and monobutylether [42].

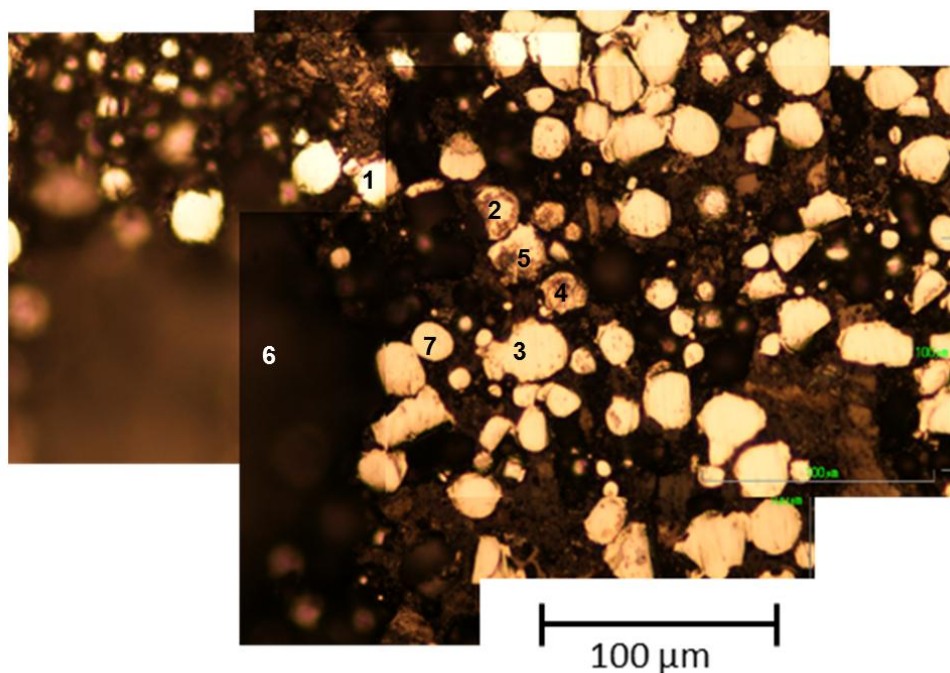


Figure 5. Optical microscopy image (of an area of polished 316L particles after exposure to 0.1 M HCl. The numbers indicate areas of EDS measurements, Table 2.

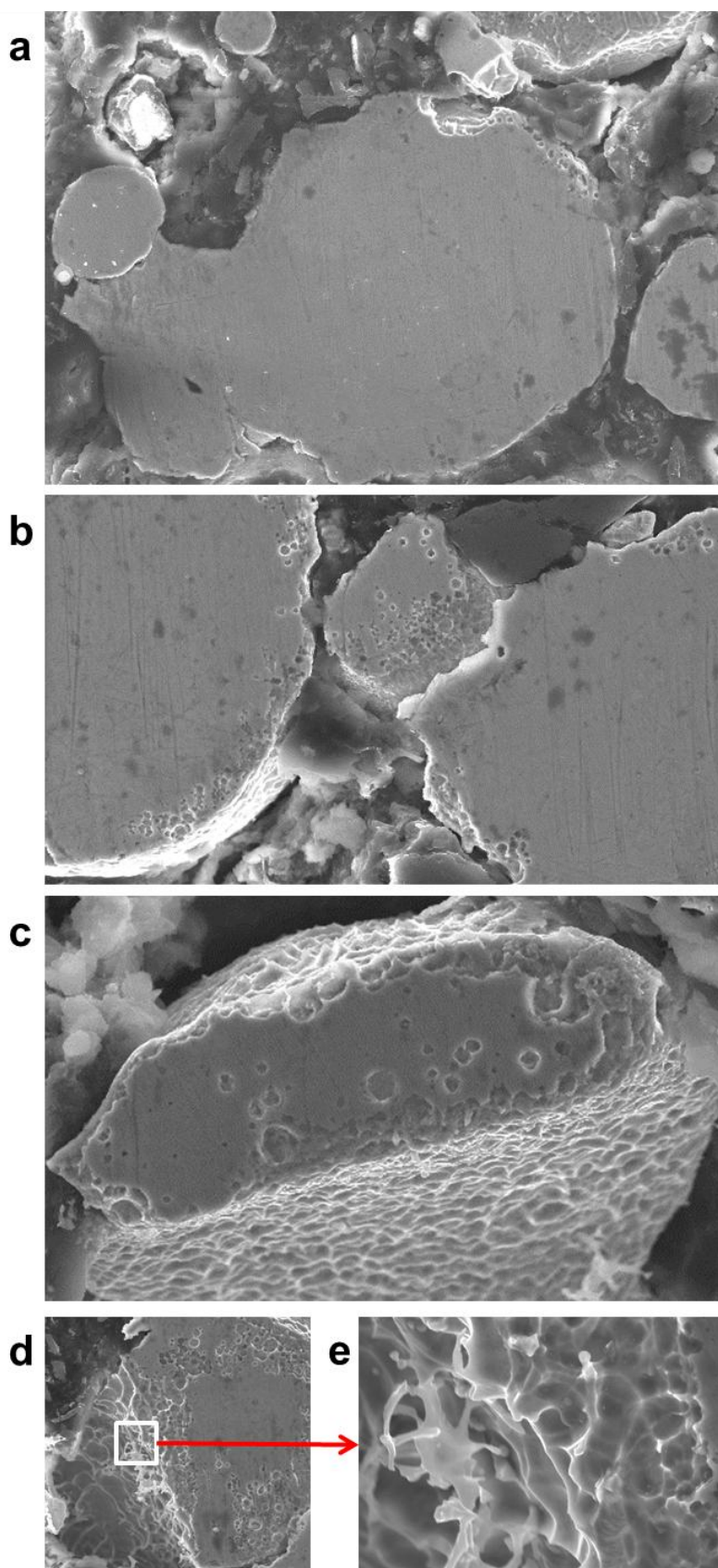


Figure 6. SEM images on selected 316L particles within the surface area displayed in Fig. 5 after micro capillary measurements a-d) Particles of increasing degree of corrosion, and e) magnification of the surface morphology of a stable pit observed in d.

Table 2. Bulk compositional measurements (wt %) of Cr, Fe and Ni by means of EDS of individual polished particles of 316L exposed to 0.1 M HCl compared to the bulk alloy composition based on supplier information.

Particle number	Cr (wt %)	Fe (wt %)	Ni (wt %)
1	18.3	71.9	9.8
2	18.4	71.5	10.1
3	17.5	71.3	11.2
4	18.2	70.9	10.9
5	18.3	71.6	10.2
6	18.7	70.9	10.4
7	18.2	71.8	10.0
Reference bulk	17.5	71.8	10.7

3.3. Corrosion of non-polished particles of the 316L powder

Micro-electrochemical investigations of non-polished inert-gas-atomized 316L powder particles are presented in Fig. 7. Duplicate measurements revealed extremely passive properties in 0.1 M HCl, without any indication of metastable or stable pitting. Since no visible corrosion attack was observed, an accurate estimation of the exposed area by comparing prior and post-measurement images was difficult. The measurements resulted in a long feature-free passive range with the typical oxidation peak after about 1000 mV, as previously discussed and assumed to predominantly be related to oxide thickening [38]. This peak was also visible for the massive 316L surface on which no stable pitting corrosion was developed (Fig. 7, included for comparison). This high passivity for non-polished particles is not surprising when comparing with macroscopic measurements of powders, which include many thousands of particles in one measurement [25-26]. Reported anodic polarization studies in similar solutions as this study (0.03 and 0.14 M HCl) did not result in any stable pitting (or dissolution of activated particles) [25-26]. However, macroscopic measurements by the authors clearly showed that these non-polished particles revealed a higher pitting corrosion susceptibility compared with other powders of the same composition, but that did not have any Mn-, Fe- and S-rich oxide nanoparticles on the surface [26, 40].

The PIGE is widely used to perform electrochemical measurements of micron-sized particles due to its low background current [31]. The measured background polarization curve (PIGE without particles) was significantly different compared with PIGE including particles. It is worth noting that the measured corrosion potential of non-polished particles (at approximately -400 mV (Ag/AgCl), Fig. 7) was very different from the open-circuit potential (+400 mV) prior to the measurement. This is in

agreement with macroscopic observations, and believed to be caused by the presence of an easily reduced oxidized Mn(III) or Mn(IV)-containing phase on the surface of these particles. The effect and importance of this phase is discussed and presented in [26]. It should be underlined that the Mn-, Fe-, and S-rich oxide nanoparticles at the particle surface of the non-polished particles [26, 40] did not seem to induce any pitting corrosion in microscopic investigations at the given conditions, an observation in contrast with polished and aged (24 h) particles. Clearly, the surface oxide of the non-polished particles is crucial for the outstanding corrosion resistance of non-polished inert-gas atomized 316L stainless steel powder particles.

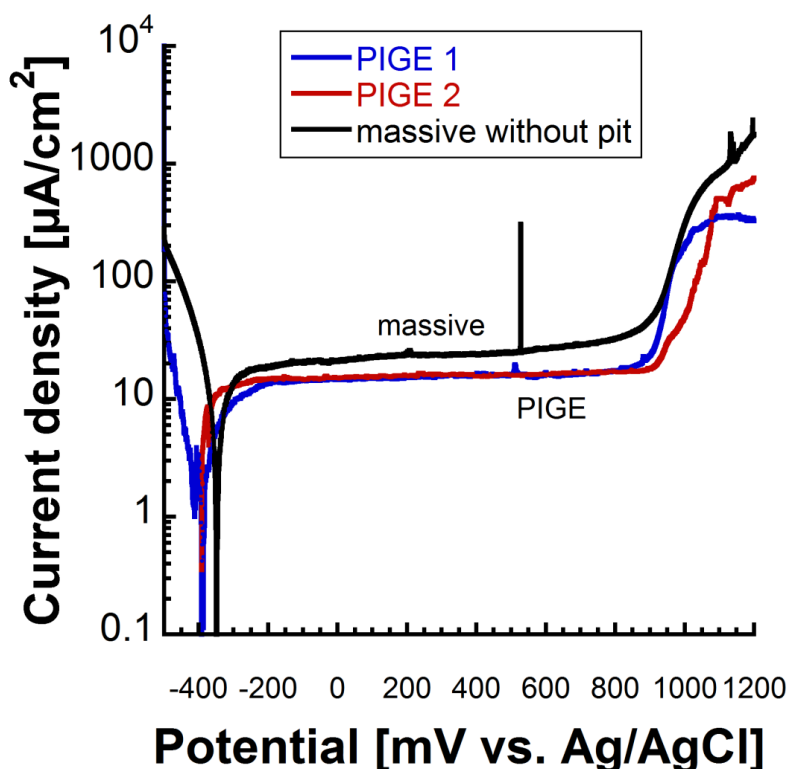


Figure 7. Current density – potential curves for two independent measurements on non-polished (as-received) 316L powder particles fixed on a PIGE substrate exposed to 0.1 M HCl. A corresponding curve for massive sheet (no pits observed, c.f. Figs. 2b and 3b) is included for comparison.

3.4. Comparison powder – massive stainless steel 316L

Current-potential curves of polished massive sheet and powder particles of 316L in 0.1 M HCl are presented in Fig. 8, divided into occasions without any observed pitting corrosion (Fig. 8a) or relatively low passive current and/or re-passivation in the case of the particles (Fig. 8c, curve 4), and occasions with pitting corrosion (Figs. 8b and 8c, curves 1-3). The results on massive 316L (Fig. 8a and b) clearly showed similar corrosion potential values, passive current densities, and transpassive current densities between different replicate measurements. Small observed differences between replicate measurements indicate a very homogeneous behavior of the massive stainless steel 316L,

except from the possible presence of surface defects initiating pitting corrosion. A large variance of the pitting potential was observed, as discussed earlier, and as a consequence, a large variation of calculated pit depths of 0-30 μm (calculation according to eq. 1, the observed pit diameter, and the assumption of a cylindrical pit shape).

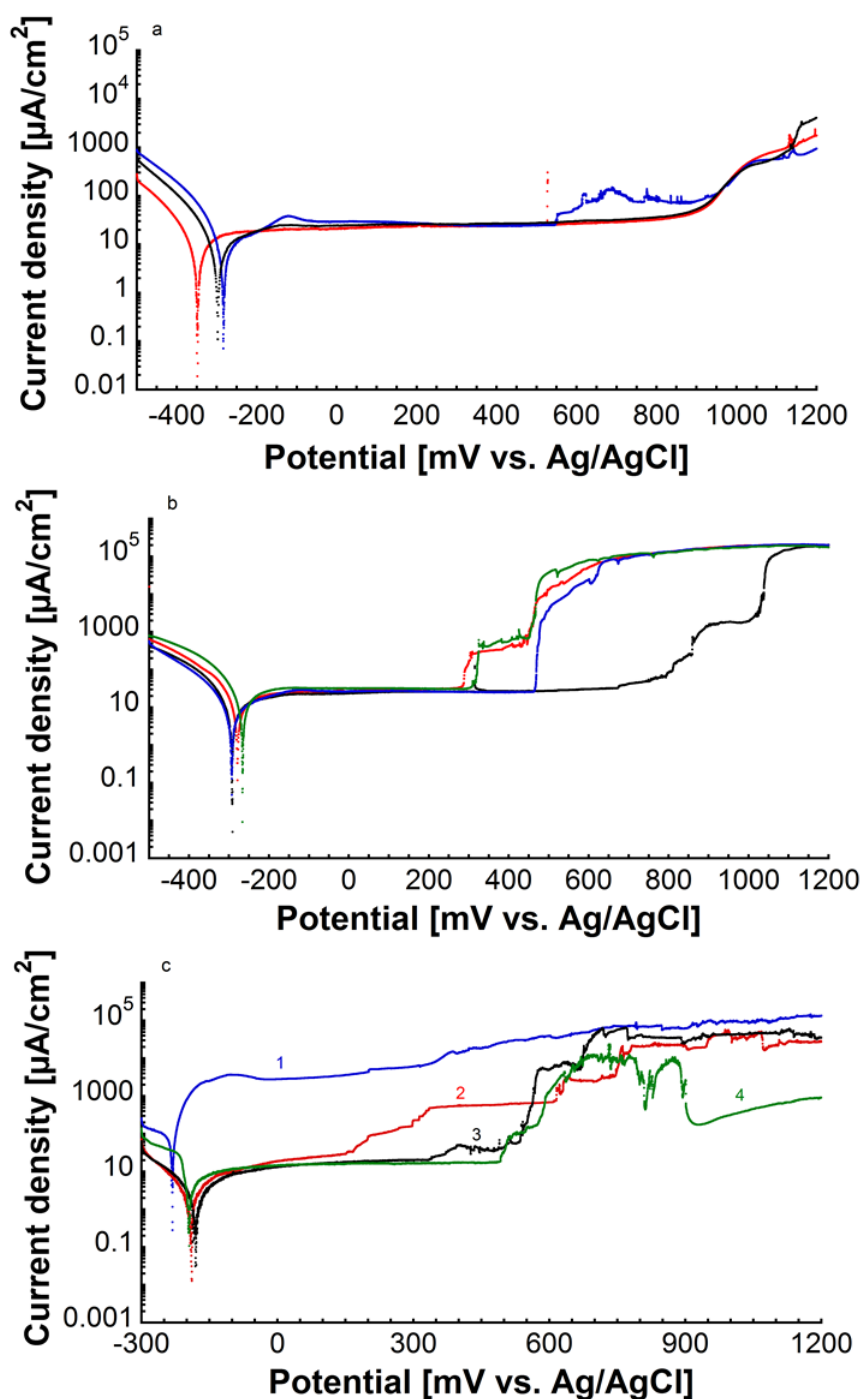


Figure 8. Current density – potential curves of polished massive sheet (a and b) and polished embedded particles (c) of 316L in 0.1M HCl. a) 3 independent measurements without any observed pitting corrosion for massive 316L; b) 4 independent (selected) measurements on massive 316L with pitting corrosion; c) 4 independent measurements on particles showing some kind of repassivation (4) and clear breakdown without repassivation (1-3).

Micro-electrochemical measurements of powder particles (Figs. 8c) compared to massive sheet (Figs. 8a and b) are more complex as they involve the conducting substrate (the resin), several individual particles (multi-system), and possible effects of crevices. Observed passive and transpassive current densities were slightly different among different particle measurements, an effect most probably related to differently exposed particle areas (not accounted for in the current density calculation, estimated being 2-5 times smaller compared with massive 316L). The major difference compared to the massive 316L, was the possibility of multi-step-breakdown and “repassivation”, i.e. the decrease in current density (possibly caused by the complete dissolution of some active particles), both related to the multi-system with several individual particles. Measured corrosion potentials for the powder particles were similar between different replicate measurements (with one exception), but were more positive (-199 ± 20 mV) compared with massive 316L (-291 ± 26 mV). This effect is believed to be a side consequence of the resin material, which has a background corrosion potential of -140 mV (Ag/AgCl) (without any particles). It could be argued that this, obviously more noble, resin may cause galvanic corrosion effects in contact with the stainless steel particles. This is not very probable as long as the stainless steel particle shows stable passivity, but possible in the presence of halides (as in this study) when pits can be initiated to a higher extent compared to the uncoupled state (stainless steel without contact to graphite) [43]. In general, polished massive 316L behaved similar to polished 316L powder particles from a corrosion perspective (Fig. 8), but very different to non-polished particles, with the exception of no pitting corrosion (Fig. 7). This is in agreement with macroscopic measurements, where very aggressive electrolytes are required to cause any pitting corrosion in the case of the powder, in contrast to the massive sheet [25-26]. Both passive and transpassive current densities were in the same range for polished massive sheet and micrometer-sized particles of 316L. The possibility of both no effects and pitting corrosion, or breakdown/repassivation-events, depending on the location of the capillary on the surface was similar in both cases. Since the particles represent several individual corrosion cells within one measurement, their total breakdown probability is higher (lower pitting potentials compared with massive 316L). This might be related to the presence of a few more active particles in the area of measurement, higher probability of the most corrosion susceptible grain orientations due to several particles exposed at the same time, their higher sulfur content compared with the massive 316L, galvanic coupling, and/or to effects of crevices.

4. CONCLUSIONS

Electrochemical measurements using a micro-capillary technique were conducted to assess differences in corrosion mechanisms between low sulfur-containing polished massive AISI 316L stainless steel and micrometer-sized particles of an inert-gas-atomized 316L powder embedded in resin (polished) or fixated to a PIGE substrate (non-polished). Generated data was compared with optical microscopy, SEM-imaging and bulk compositional analysis using EDS on the same area. The following main conclusions are drawn:

1. The combination of micro-capillary electrochemical measurements and microscopic imaging enables a novel possibility for studies of corrosion processes on single micrometer-sized particles.
2. Non-polished 316L particles were significantly more passive in 0.1 M HCl compared to polished massive sheet and polished particles of 316L, which revealed in general similar corrosion behavior.
3. Pitting corrosion on the particles was not induced by differences in bulk composition between different particles. Once pitting was initiated, pit propagation was favorable compared with initiation of new pits.
4. Corrosion of polished 316L particles, approximately sized 20 μm and embedded in resin, was induced by pitting (possibly crevice corrosion), an effect that occurred more or less independently of the location of the particle within the capillary area, or of its distance to other corroding particles.

ACKNOWLEDGEMENTS

Financial support of Yolanda Hedberg from Cusanuswerk, Germany, and travel grants from the Swedish Steel Association (Jernkontoret) and the Björn Foundation at KTH, Royal Institute of Technology, Sweden, are gratefully acknowledged.

Florian Seuss, Dr. Johannes Brunner, and Leonhard Klein at University of Erlangen-Nuremberg are highly acknowledged for experimental help.

Yolanda Hedberg and Inger Odnevall Wallinder are members of the Stockholm Particle Group, an operative network between three universities in Stockholm: Karolinska Institutet, Royal Institute of Technology and Stockholm University, supported by the Swedish Research Councils VR and Formas.

References

1. A. J. Sedriks: *Corrosion of Stainless Steels*, John Wiley & Sons, Inc., New York (1996).
2. J. Pan, C. Karlen, and C. Ulfvin, *J. Electrochem. Soc.*, 147(3) (2000) 1021.
3. A. Shahryari, J. A. Szpunar, and S. Omanovic, *Corros. Sci.*, 51(3) (2009) 677.
4. P. Marcus, V. Maurice, and H. H. Strehblow, *Corros. Sci.*, 50(9) (2008) 2698.
5. G. Frankel, *J. Electrochem. Soc.*, 145(6) (1998) 2186.
6. U. Steinsmo and H. S. Isaacs, *Corros. Sci.*, 35(1-4) (1993) 83.
7. G. S. Frankel, L. Stockert, F. Hunkeler, and H. Boehni, *Corrosion*, 43(7) (1987) 429.
8. H. P. Leckie and H. H. Uhlig, *J. Electrochem. Soc.*, 113(12) (1966) 1262.
9. J. Galvele, *Corros. Sci.*, 21(8) (1981) 551.
10. J. Mankowski and Z. Szklarska-Smialowska, *Corros. Sci.*, 15(6-12) (1975) 493.
11. N. Pessall and C. Liu, *Electrochim. Acta*, 16(11) (1971) 1987.
12. Y. Kobayashi, S. Virtanen, and H. Bohni, *J. Electrochem. Soc.*, 147(1) (2000) 155.
13. S. Haupt and H. H. Strehblow, *Corros. Sci.*, 29(2-3) (1989) 163.
14. H. Böhni, T. Suter, and A. Schreyer, *Electrochim. Acta*, 40(10) (1995) 1361.
15. M. P. Ryan, R. C. Newman, and G. E. Thompson, *Philos. Mag. B*, 70(2) (1994) 241.
16. M. P. Ryan, R. C. Newman, and G. E. Thompson, *J. Electrochem. Soc.*, 141(12) (1994) L164.
17. H. Nanjo, R. C. Newman, and N. Sanada, *Appl. Surf. Sci.*, 121-122(0) (1997) 253.
18. G. Herting, I. Odnevall Wallinder, and C. Leygraf, *Corros. Sci.*, 49(1) (2007) 103.

19. Y. Hedberg, J. Gustafsson, H. L. Karlsson, L. Möller, and I. Odnevall Wallinder, *Part. Fibre Toxicol.*, 7:23 (2010).
20. Y. Hedberg, J. Hedberg, Y. Liu, and I. Odnevall Wallinder, *BioMetals*, 24(6) (2011) 1099.
21. K. Midander, A. de Frutos, Y. Hedberg, G. Darrie, and I. Odnevall Wallinder, *Integrat. Environ. Assess. Manag.*, 6(3) (2010) 441.
22. Y. Hedberg, K. Midander, and I. Odnevall Wallinder, *Integrat. Environ. Assess. Manag.*, 6(3) (2010) 456.
23. Y. Hedberg, O. Karlsson, P. Szakalos, and I. Odnevall Wallinder, *Mater. Lett.*, 65(14) (2011) 2089.
24. K. Midander, J. Pan, I. Odnevall Wallinder, and C. Leygraf, *J. Environ. Monitor.*, 9 (2007) 74.
25. C. Baldizzone: *Investigations of passivity and reactivity of alloy particles, effects of sonication and particle size*, PhD thesis, Royal Institute of Technology (KTH), Stockholm, 2010.
26. Y. Hedberg, P. Linhardt, H. Bergqvist, M. Norell, and I. Odnevall Wallinder, *Int. J. Electrochem. Sci.*, in press (previous article in this issue).
27. T. Suter and H. Böhni, *Electrochim. Acta*, 47(1–2) (2001) 191.
28. H. Böhni, T. Suter, and F. Assi, *Surf. Coat. Tech.*, 130(1) (2000) 80.
29. T. Suter and H. Böhni, *Electrochim. Acta*, 42(20–22) (1997) 3275.
30. A. Doménech, M. T. Doménech-Carbó, T. Pasies, and M. C. Bouzas, *Electroanal.*, 23(12) (2011) 2803.
31. F. Scholz, U. Schröder, and R. Gulaboski: *Electrochemistry of immobilized particles and droplets*, Springer Verlag, (2005).
32. T. Grygar, P. Bezdicka, D. Hradil, A. Domenech-Carbo, F. Marken, L. Pikna, and G. Cepria, *Analyst*, 127(8) (2002) 1100.
33. T. Suter and H. Böhni, *Electrochim. Acta*, 43(19–20) (1998) 2843.
34. G. Wranglen, *Corros. Sci.*, 14(5) (1974) 331.
35. P. Schmuki, H. Hildebrand, A. Friedrich, and S. Virtanen, *Corros. Sci.*, 47(5) (2005) 1239.
36. J. E. Castle and R. Ke, *Corros. Sci.*, 30(4-5) (1990) 409.
37. D. E. Williams, M. R. Kilburn, J. Cliff, and G. I. N. Waterhouse, *Corros. Sci.*, 52(11) (2010) 3702.
38. V. Maurice, W. P. Yang, and P. Marcus, *J. Electrochem. Soc.*, 145(3) (1998) 909.
39. L. L. Shreir: *Corrosion - Metal/Environment Reactions*, Butterworth Heinemann, (1994).
40. Y. Hedberg, P. Linhardt, M. Norell, J. Hedberg, P. Szakálos, and I. Odnevall Wallinder, *Powder Metall.*, in press.
41. N. Aouina, F. Balbaud-Célérier, F. Huet, S. Joiret, H. Perrot, F. Rouillard, and V. Vivier, *Electrochim. Acta*, 56(24) (2011) 8589.
42. V. Vignal, J. C. Roux, S. Flandrois, and A. Fevrier, *Corros. Sci.*, 42(6) (2000) 1041.
43. L. H. Hihara and R. M. Latanision, *Int. Mater. Rev.*, 39(6) (1994) 245.